Results and applications of SiPM photodetectors from FBK-irst by the DASIPM Collaboration(*)

A. Del Guerra[1], G. Collazuol[1], G. Llosá[1], S. Marcatili[1],
C. Piemonte[2], G-F. Dalla Betta[3], G. Ambrosi[4], R. Battiston[4],
M. Ionica[4], G. Levi[5], F. Corsi[6], C. Marzocca[6], G. Matarrese[6]
and M. Foresta[6]

[1] Università di Pisa and INFN, Sezione di Pisa - Largo B. Pontecorvo 3, Pisa, Italy
[2] FBK-irst - Via Sommarive 18, I-38050 Povo di Trento, Italy
[3] Università di Trento and INFN, Sezione di Padova (Gruppo collegato di Trento)
    Via Sommarive 14, I-38050 Povo di Trento, Italy
[4] Università di Perugia and INFN, Sezione di Perugia - I-06123 Perugia, Italy
[5] Università di Bologna and INFN, Sezione di Bologna - Viale Pichat, 40127 Bologna, Italy
[6] DEE-Politecnico di Bari and INFN, Sezione di Bari - Via Orabona 4, I-70125 Bari, Italy

Summary. — Silicon Photomultipliers (SiPMs) and SiPM matrices optimized for the detection of blue light have been developed at FBK-irst. The first devices produced are composed of 625 microcells with $40\,\mu\text{m} \times 40\,\mu\text{m}$ size, in a $1\,\text{mm} \times 1\,\text{mm}$ active area. The devices have a breakdown voltage around $30\,\text{V}$, and a gain about 10^6. The DASIPM Collaboration is evaluating their performance and possible applications in high-energy physics, space physics and medical imaging. Dedicated front-end electronics are also being developed.

PACS 85.60.Gz – Photodetectors (including infrared and CCD detectors).

1. – Introduction

The improved properties of SiPMs with respect to other vacuum and solid-state photodetectors have raised their interest in the last few years.

The first devices produced by FBK-irst have a size of $1\,\text{mm} \times 1\,\text{mm}$ and are composed of 25×25 microcells of $40\,\mu\text{m} \times 40\,\mu\text{m}$ size [1] (fig. 1 left). The quenching resistor of the microcells is implemented by a mildly-doped polysilicon layer. These SiPMs are fabricated on p-type $4\,\mu\text{m}$ thick epitaxial substrates and the diodes implant profiles are optimized to maximize the detection efficiency in the blue region. A special anti-reflective coating is implemented on top of the diodes to maximize the light transmission at wavelengths

---
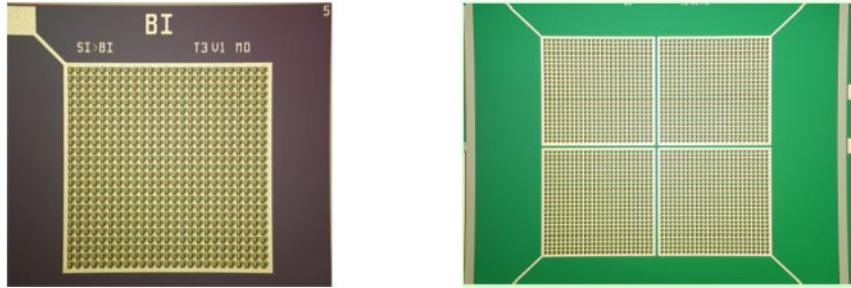
Fig. 1. – Left: single SiPM, $1\,\mathrm{mm} \times 1\,\mathrm{mm}$ active area, fabricated at FBK-irst. Right: SiPM matrix composed of four (2×2) $1\,\mathrm{mm} \times 1\,\mathrm{mm}$ SiPM elements in a common substrate.

around 420–450 nm, that correspond to the maximum emission of the LYSO scintillator crystal. The first SiPM matrix test structures are composed of four SiPM elements of the same characteristics in a common substrate (fig. 1 right).

Recently, new devices with improved characteristics and different geometries have been produced. The new devices have reduced noise and higher active area, that results in a higher Photon Detection Efficiency (PDE) [2].

In the following sections, the main results achieved with the first SiPMs produced at FBK-irst will be presented.

2. – Results

The main results of the optical characterization of the devices, noise, gain, temperature dependence and timing are shown in this section. The performance of single SiPMs and the first SiPM matrices as photodetectors for scintillators has also been evaluated, and the results will be presented. In addition, tests in a magnetic resonance system have been performed, showing no degradation of the data taken when SiPMs are under the influence of static and gradient fields [3]. Studies on radiation hardness are being carried out.
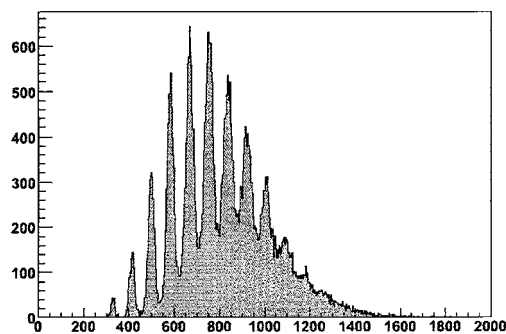

Fig. 2. – Single photoelectron spectrum obtained illuminating the SiPM with low-intensity light pulses from an LED.
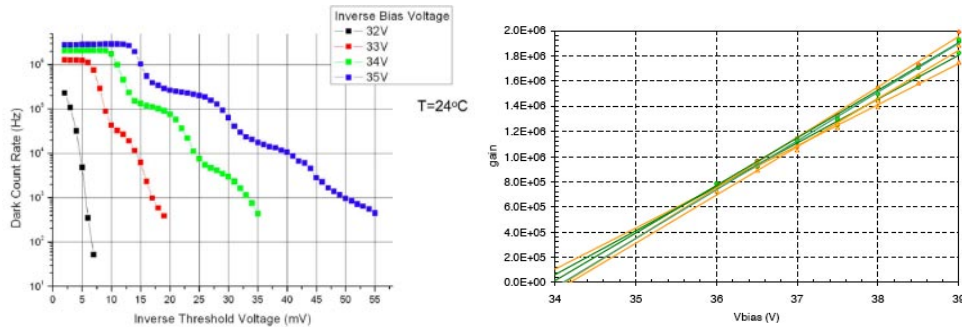
Fig. 3. – Left: dark rate spectrum at different values of the bias voltage. Right: gain as a function of the bias voltage for several devices.

2˙1. *Characterization results.* – The samples fabricated in the first runs showed very uniform values in the breakdown voltage and the current (breakdown voltage uniformity within 1 V), which confirms the feasibility of large-area arrays [4]. Single photoelectron spectra have been acquired illuminating the device with an LED. Figure 2 shows the histogram of the charge measured during short, low-intensity light flashes at room temperature and at an overvoltage (bias voltage exceeding the breakdown value) of 2 V. The spectrum shows the peaks corresponding to 1 to 9 measured photoelectrons. Such well-resolved single photoelectron peaks are due to the large signal-to-noise ratio.

The single-electron dark count of the tested devices (fig. 3 left) is in the order of 1–3 MHz at 1.5–3.5 V above the breakdown voltage, a value which is similar to that reported in the literature by other producers. The dark count value for double or higher peaks drops down dramatically to kHz as the threshold is increased to 3-4 photoelectrons level. These results correspond to SiPM prototypes that do not feature optical isolation between the cells. Still the optical cross-talk is low. Devices featuring optical trenches to ensure optical isolation have also been produced and tested, showing that this structure is not necessary.

The gain has been calculated by the separation of the single photoelectron peaks, yielding values around 10^6, and increasing linearly with the overvoltage. The results for several devices are shown in fig. 3 (right). Again, the uniformity in this results confirms the reproducibility of the device characteristics and the feasibility of the matrices.

2˙2. *Intrinsic time resolution.* – Intrinsic timing measurements have been carried out at the photoelectron level, employing a laser emitting 60 fs pulses at 80 MHz rate (*i.e.* $T = 12.34$ ns) with less than 100 ps jitter [5]. Two wavelengths were tested, 400 ± 7 nm and 800 ± 15 nm. The analysis of the data estimates the time difference of contiguous signals corresponding to 1 p.e. The time difference distribution is fitted with a Gaussian function. A timing resolution around 60 ps sigma is obtained for 3–4 V overvoltage and blue light. The values obtained for red light are slightly (about 10%) higher, due to the depth at which the interaction is produced (fig. 4 left). In addition, the timing dependence on the square root of the number of photoelectrons has been checked up to 15 photoelectrons, at which the measured intrinsic time resolution is 20 ps sigma (fig. 4 right).
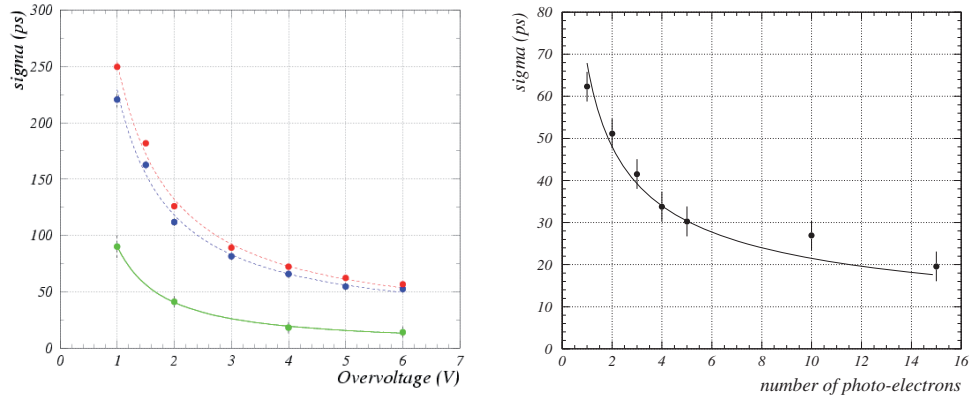
Fig. 4. – Left: intrinsic time resolution as a function of the overvoltage for two different wavelengths: 800 nm (upper curve) and 400 nm (middle curve). The lower curve is the estimated contribution of the electronics noise and the evaluation method, that has not been subtracted. Right: dependence on the number of photoelectrons detected. The noise contribution has been subtracted.

2˙3. *Temperature dependence*. – The temperature dependence of the SiPM properties has also been evaluated. Figure 5 left shows the variation of the leakage current with bias voltage at different temperatures. At a bias voltage over the breakdown (overvoltage) of about 5 V, the leakage current is reduced from about 1 μA at room temperature (300 K) to 100 nA at 230 K. In fig. 5 right, the relative variation of the breakdown voltage with respect to its value at room temperature (300 K) is plotted for different values of the temperature. The change in the breakdown voltage is due to the decrease of the probability that an avalanche is produced when the temperature increases due to the reduction of the mean free path. A variation of about 30 mV per Kelvin has been found. The variation of the gain with the bias voltage has also been evaluated, finding a change
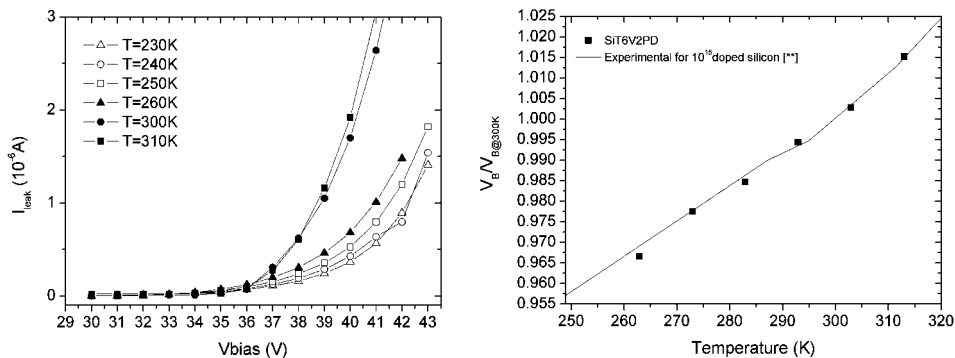

Fig. 5. – Temperature dependence of the leakage current (left) and of the breakdown voltage (right).
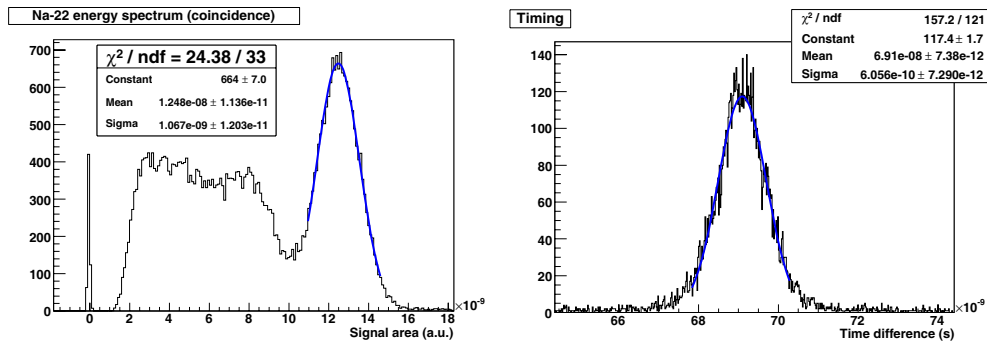
Fig. 6. – Left: ^{22}Na energy spectrum obtained with a LSO crystal coupled to a SiPM. The energy resolution is 20%. Right: coincidence timing resolutions of two SiPMs coupled to LSO crystals. The timing resolution is 600 ps sigma.

of about 4% per degree. However, if the change in the breakdown voltage is taken into account in these results, for a given voltage no variation of the gain with temperature is observed, proving that the variation of the gain is mainly due to the change in the breakdown voltage.

2˙4. *Energy resolution*. – The SiPM performance as photodetector for scintillators has also been tested. The set-up employed consists of two $1 \, \text{mm} \times 1 \, \text{mm} \times 1 \, \text{cm}$ LSO crystals coupled to two SiPMs and operated in time coincidence. The signals coming from each of the SiPMs are split and sent both to a discriminator, and to a QDC for integration. The time coincidence of the discriminated signals produces the integration gate for the QDC. An integration time of 240 ns was employed. Figure 6 left shows a ^{22}Na spectrum obtained. The fit of the photopeak gives an energy resolution of 20% FWHM.

2˙5. *Coincidence timing resolution*. – Coincidence timing measurements have also been carried out with the set-up described in the previous section and a ^{22}Na source. In this case, the signals corresponding only to full energy events are selected, raising the threshold to record only those events corresponding to the 511 keV photopeak. The time difference between the signals coming from the two SiPMs is plotted and fitted with a Gaussian function. The coincidence time resolution measured is 600 ps sigma (fig. 6 right).

2˙6. *Results with SiPM matrices*. – The first matrices consisting of a 2×2 array of SiPMs in the same substrate (fig. 1 right) have also been tested. A ^{22}Na energy spectrum has been obtained placing a small ($1 \, \text{mm} \times 1 \, \text{mm} \times 10 \, \text{mm}$) LSO crystal in the center of the matrix, and summing the signals from the four pixel elements for each event. In this case, the energy resolution, of 30% FWHM (fig. 7 left) is worse than for single SiPMs due to the smaller active area of the SiPMs that integrate the matrix. If the energy resolution of a SiPM with the same characteristics of the SiPMs in the matrix is evaluated independently, the same energy resolution is obtained, showing that the energy resolution is not degraded by the fabrication or operation of the SiPM matrices.

2˙7. *New detectors*. – New devices have recently been produced and are being tested [2]. The devices have reduced noise with respect to previous runs, and higher geometrical efficiency (44–50%). In addition, different sizes and geometries, such as SiPMs
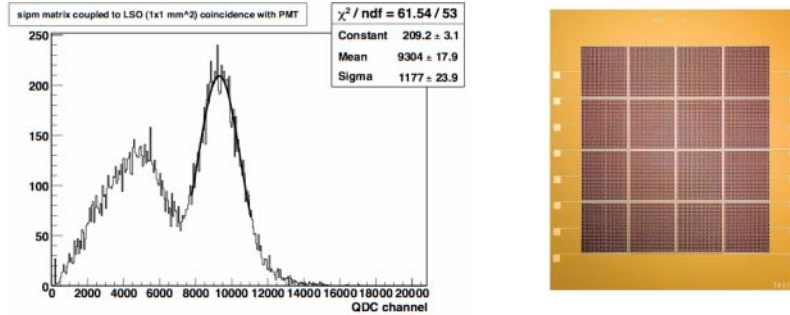
Fig. 7. – Left: ^{22}Na energy spectrum obtained placing a LSO crystal in the center of a 2×2 SiPM matrix and adding the signals from the four SiPMs. Right: SiPM matrix with 16 (4×4) SiPM pixel elements in a common substrate recently fabricated at FBK-irst.

of dimensions $1\,\mathrm{mm} \times 1\,\mathrm{mm}$, $2\,\mathrm{mm} \times 2\,\mathrm{mm}$, $3\,\mathrm{mm} \times 3\,\mathrm{mm}$ (3600 microcells), $4\,\mathrm{mm} \times 4\,\mathrm{mm}$ (6400 microcells), and circular SiPMs of 1 mm diameter, and a different microcell size of $50\,\mu\mathrm{m} \times 50\,\mu\mathrm{m}$ have been developed. Arrays of 8, 16 or 32 SiPMs of $0.250\,\mathrm{mm} \times 1\,\mathrm{mm}$ size have also been produced. This run also includes matrices of 16 (4×4) SiPM elements of $1\,\mathrm{mm} \times 1\,\mathrm{mm}$ size (fig. 7 right). Very preliminary measurements have been carried out with the devices. The first ^{22}Na energy spectra produced with the matrices gives an energy resolution of 20% FWHM for the 511 keV peak, that is better than the previous matrices developed, mainly due to the increase of the active area of the microcells up to 44%.

3. – Electronics development

A readout system based on a dedicated front-end ASIC is under development, in order to optimize it for the readout of the SiPM matrices. The excellent signal-to-noise ratio of SiPMs makes the use of sophisticated low-noise preamplifiers unnecessary. However, the ASIC channel input stage must be fast enough to cope with the excellent timing properties of the detector, while the dynamic range needs to be tailored to the maximum charge expected. Since noise is not the main problem in the SiPM case, due to the remarkable amount of charge generated by an event, different architectures can be possibly adopted. Therefore a preliminary study about the most suitable approach for an optimal integrated front-end circuit is mandatory [6]. The availability of an accurate electrical model of the SiPM is of great help for this purpose, since reliable simulations at circuit level of the detector coupled to the front-end electronics can be performed. We developed a realistic model of the SiPM, which is similar to the classical one [7], but includes parasitic elements which have been estimated to be not negligible with simple considerations based on the typical values of technological and geometrical parameters.

The definition of the front-end architecture has been based on a previous study of the electrical characteristics (both static and dynamic) of the SiPM as a signal source. In particular, the shape of the current pulse and its maximum amplitude, for various types of scintillator crystals, has been considered in order to evaluate the dynamic range and the bandwidth of the preamplifier. The considerable difference between the minimum (few microcells fired) and maximum charge (all microcells fired) expected (1.6×10^{-13} C to 1.6×10^{-10} C) could be of some concern in the design of an integrated charge-sensitive preamplifier. In fact, in the case of maximum charge, to cope with the limits imposed
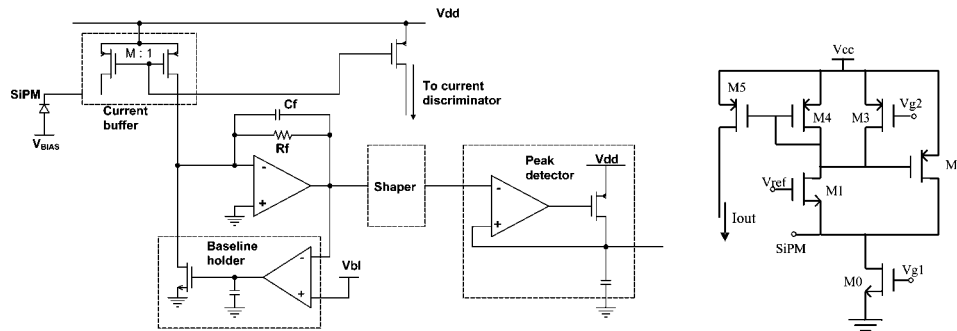
Fig. 8. – Left: architecture of the analog front-end for the SiPM; right: schematic of the current buffer.

by the output dynamic range of the amplifier (which is assumed to be a few volts), an integration capacitor of more than $50\,\mathrm{pF}$ should be used. This results to be impractical in an integrated front-end chip with hundreds of channels. For this reason, a current buffer has been chosen as input stage, which will transform the output impedance of the SiPM into a well-controlled one, while providing also a possible variable gain. In this way, besides obtaining a fast front-end circuit, thanks to the absence of high-impedance nodes, no limits are imposed on the signal dynamic range. In fact, the current mode operation appears to be the most suitable one to be implemented by a low-voltage deep submicron CMOS technology characterized by a limited headroom for the voltage swings.

The architecture of each individual channel, shown in fig. 8, will be formed by a fast signal path, containing a current discriminator which will provide the timing information needed for the coincidence analysis and for the ADC, and a slower path, passing through the peak detector. Figure 8 left shows the SiPM front-end architecture; the input block has been designed as a current buffer with very low input resistance, which allows to obtain very fast timing, high dynamic range, and maximum flexibility in the further processing of the output current. The current buffer (see fig. 8 right) is characterized by the presence of a feedback loop, used to decrease the input resistance of the front-end and increase its bandwidth. Much care has been devoted to make sure that the conditions for the stability of these loops are fulfilled. This solution guarantees a larger linearity range, besides the possibility of fine tuning the input bias, obtained by varying the voltage Vrif at the gate of the input transistor. One of the output branches of the current buffer is sent to the current discriminator to extract the timing signal which will be used for the coincidence analysis. Another output branch current, with a suitable scaling-down factor M, is integrated by means of a Charge Sensitive Amplifier (CSA) with integration time constant equal to $R_F C_F$ to extract the charge information. The baseline holder is needed to control the DC value at the output of the CSA. Possibly, a shaping amplifier could be inserted to optimize the noise performance of the circuit. Last, a peak detector is in charge of holding the maximum value of the output waveform, which is proportional to the total charge delivered by the detector.

The circuit in fig. 8 right has been realized in a $0.35\,\mu\mathrm{m}$ standard CMOS technology and some preliminary tests have been performed. On the test board, the output current of the buffers is converted into a voltage by means of a $100\,\Omega$ resistor. This voltage signal is then amplified 8 times and sent to the oscilloscope. A SiPM produced by FBK-irst (625 microcells) and a pulsed blue-light LED source have been used for the tests. Figure 9
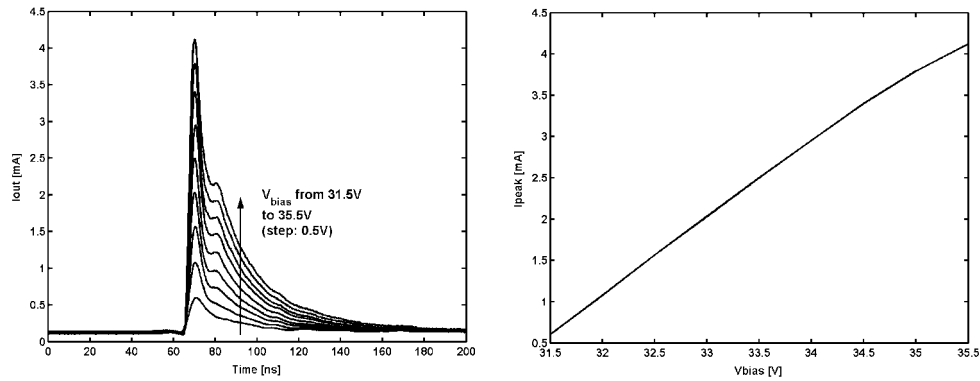
Fig. 9. – Left: response of the circuit to a LED pulse at different bias voltages; right: peak of the current response of the circuit as a function of the bias voltage.

left reports the response of the circuit to a pulse of duration 8 ns applied to the LED, at different values of the SiPM bias voltage. The light emitted by the LED is always the same in all the measurements shown, since the excitation conditions of the diode have not been changed. It should be noticed that these measurements refer to a case in which all the micro-cells of the SiPM are excited, due to the large amount of light provided by the LED used. The standard deviation of the pulse amplitude has been evaluated and it has been found equivalent to about one half of the signal delivered by a single hit micro-cell, *i.e.* half a photoelectron, which is a result in agreement with the noise level estimated by the simulations. Figure 9 right shows the peak of the signal in fig. 9 left as a function of the bias of the SiPM. As expected, the circuit exhibits good linearity performance even at high bias voltages, thus, it is able to process a large amount of charge.

The speed capabilities of the circuit have also been evaluated. The rise time of the circuit response to a single dark pulse is about 800 ps. Figure 10 shows an example of this response.
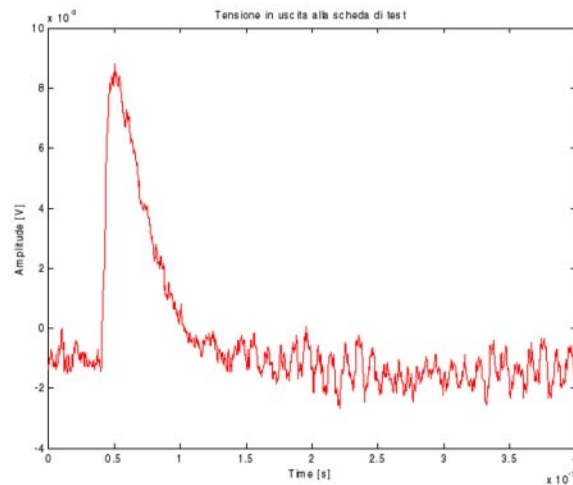

Fig. 10. – Response of the current buffer to a single dark pulse of the SiPM.
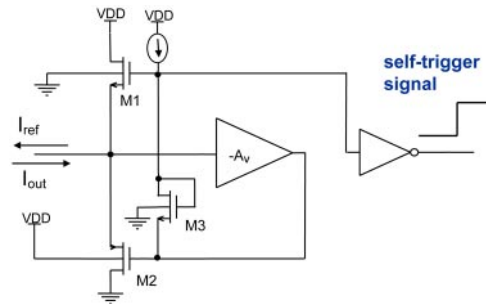
Fig. 11. – Schematic of the current discriminator.

The current discriminator is shown in fig. 11. The threshold is set by choosing the value of the current I_{REF}, for instance by means of a DAC. The rise time of the simulated output voltage is about 300 ps. The average delay of the output pulse with respect to the input current pulse is about 1.2 ns, with a maximum variation of 200 ps when the threshold is varied from its minimum to its maximum value.

The CSA has been designed to provide an integration time constant $R_F C_F$ of 200 ns, suitably larger than the recovery time constant of the micro-cells of the SiPM used. With a de-multiplication factor of the current buffer M equal to 10, corresponding to an equivalent input noise level still negligible, the value of the feedback capacitance C_F can be a reasonable 2 pF, which gives the maximum output voltage swing ($\cong 2.7$ V for the chosen $0.35\,\mu$m CMOS technology), with about 300 SiPM micro-cells hit ($V_{\mathrm{bias}} \cong 35$ V, detector occupancy 50% and total charge $\cong 2.7$ pC). Figure 12 shows the simulated output of the CSA+baseline holder corresponding to the maximum input charge of about 52.7 pC. The baseline holder sets the output DC voltage at 300 mV.

4. – Applications

The DASIPM Collaboration is evaluating the performance of the SiPMs produced by FBK-irst for different applications in high-energy physics, space physics and medical imaging. As an application to space physics, SiPMs will be tested in the Time-Of-Flight (TOF) detector of AMS02. SiPMs can offer important advantages in this field, where their reduced size and weight and low power consumption, as well as their insensitivity to
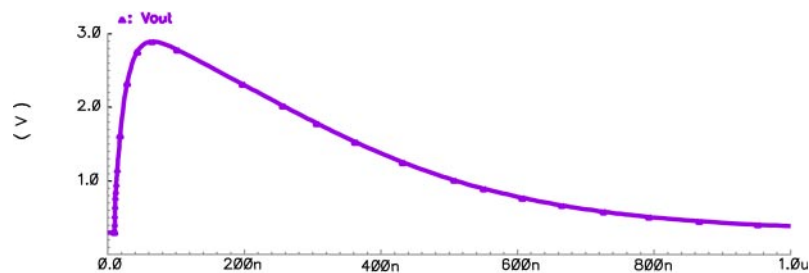

Fig. 12. – Simulated output response of CSA+baseline holder block.

magnetic fields are critical issues. Their fast response is also essential for TOF applications [8]. SiPMs will also be evaluated for a scintillating fiber tracker, where Visible-Light photon counters (VLPC) can be replaced by SiPMs that have high gain and need no or moderate cooling. The application of SiPMs to medical imaging is also being evaluated. In this field, the development of SiPM matrices is mandatory to maximize the active area of the photodetector. A PET detector employing SiPMs for scintillator readout has been proposed [9] and is under construction. The tomograph consists of four $4\,\text{cm} \times 4\,\text{cm}$ detector heads that rotate around the object to be imaged. A detector head is made of a stack of three layers. Each layer is composed of a 5 mm thick scintillator slab read out by a SiPM matrix structure, with $1\,\text{mm} \times 1\,\text{mm}$ pixels in a 1.5 mm pitch. The total scintillator thickness is 15 mm, ensuring a high detection efficiency for 511 keV photons, while the three-layer structure provides discrete depth of interaction information that reduces the parallax error and improves the spatial resolution. The use of continuous scintillators instead of pixellated blocks allows to improve the spatial resolution, while avoiding the problems of light collection efficiency that are related to fine pixellation of the crystals. Additionally, the cost of the detector is reduced. According to simulations carried out with Geant4 [10] and taking into account the characteristics of the FBK-irst photomultipliers, an intrinsic spatial resolution of 0.3 mm FWHM, and 70% efficiency can be obtained for a detector head. For the full tomograph a spatial resolution well below 1 mm at the center of the field of view employing filtering backprojection algorithms is expected for ^{18}F.

SiPMs can be employed for other interesting PET applications. Their high intrinsic time resolution makes them the optimum photodetector for TOF PET, if fast scintillators, such as LuI$_3$, become available. In this application, the time difference between the two coincidence events is employed to improve the determination of the positron origin. The combination of morphological and structural imaging technologies is essential to provide an anatomical reference for the functional data. The combination of PET and CT imaging modalities has been achieved. However, the combination of PET and MRI would allow a much improved resolution and avoid the radiation dose due to CT. Existing approaches result in a degraded performance for PET and MR images. SiPMs can overcome the two main limitations for the combination of PET and MR imaging technologies: the space constraint inside the magnet, and the sensitivity of PMTs to magnetic fields. The development of a PET insert based on SiPMs to be operated inside a small animal MR scanner that will allow simultaneous PET/MR imaging is also being studied at the University of Pisa [3].

5. – Conclusions

The performance of the first SiPMs and SiPM matrices fabricated by FBK-irst has been evaluated, and very good results have been achieved. FBK-irst has recently produced new devices with different sizes and geometries. The application of SiPMs to high-energy physics, space physics and medical imaging is under study.

REFERENCES

[1] PIEMONTE C., *Silicon avalanche photodiodes on the base of metal-resistor-semiconductor (MRS) structures*, Nucl. Instrum. Methods A, **568** (2007) 224.
[2] PIEMONTE C. *et al.*, *Recent developments on Silicon Photomultipliers produced at FBK-irst*, in *2007 IEEE NSS MIC Conf. Rec.*, CD ROM, ISBN 1-4244-0923-3, N41-2, pp. 2089-2092.

[3] HAWKES R. *et al.*, *Silicon Photomultiplier performance tests in magnetic resonance pulsed fields*, in *2007 IEEE NSS MIC Conf. Rec.*, CD ROM, ISBN 1-4244-0923-3, M18-8, pp. 3400-3403.

[4] PIEMONTE C. *et al.*, *Characterization of the first prototypes of Silicon Photomultiplier fabricated at ITC-irst*, *IEEE Trans. Nucl. Sci*, **54** (2007) 236.

[5] COLLAZUOL G. *et al.*, *Single photon timing resolution and detection efficiency of the IRST Silicon Photo-multipliers*, *Nucl. Instrum. Methods A*, **581** (2007) 461.

[6] CORSI F., MARZOCCA C. *et al.*, *Electrical Characterization of Silicon Photo-Multiplier Detectors for Optimal Front-End Design*, in *2006 IEEE NSS Conf. Rec.*, CD ROM, ISBN 1-4244-0561-0, N30-222, pp. 1276-1280.

[7] PAVLOV N., MAEHLUM G. and MEIER D., *Gamma Spectroscopy using a Silicon Photomultiplier and a Scintillator*, in *2005 IEEE NSS Conf. Rec.*, CD ROM, ISBN 0-7803-9221-3, N9-3, pp. 173-180.

[8] AGOSTINELLI S. *et al.*, *Preliminary Study of Silicon Photomultipliers for Space Missions*, *Nucl. Instrum. Methods A*, **572** (2007) 662.

[9] MOEHRS S. *et al.*, *A detector Head design for small animal PET with silicon photomultipliers (SiPM)*, *Phys. Med. Biol.*, **51** (2006) 1113.

[10] AGOSTINELLI S. *et al.*, *Geant4 - a simulation toolkit*, *Nucl. Instrum. Methods A*, **506** (2003) 250.